Tectonophysics 839 (2022) 229546

Contents lists available at ScienceDirect

Tectonophysics

journal homepage: www.elsevier.com/locate/tecto

3D geomechanical modeling of the Xianshuihe fault zone, SE Tibetan Plateau: Implications for seismic hazard assessment

Xianrui Li [a], Ke Gao [a,b,*], Yu Feng [a,c], Chongyuan Zhang [d,e]

[a] Department of Earth and Space Sciences, Southern University of Science and Technology, Shenzhen 518055, Guangdong, China
[b] Guangdong Provincial Key Laboratory of Geophysical High-resolution Imaging Technology, Southern University of Science and Technology, Shenzhen 518055, Guangdong, China
[c] Institute of Risk Analysis, Prediction and Management (Risks-X), Academy for Advanced Interdisciplinary Studies, Southern University of Science and Technology, Shenzhen 518055, Guangdong, China
[d] School of Mechanics and Civil Engineering, China University of Mining and Technology, Beijing 100083, China
[e] Key Laboratory of Neotectonic Movement and Geohazard, Institute of Geomechanics, Chinese Academy of Geological Sciences, Beijing 100081, China

ARTICLE INFO

Keywords:
Xianshuihe fault
Kinematics
Stress
Geomechanical model
Seismic hazard

ABSTRACT

The Xianshuihe fault on the southeastern margin of the Tibetan Plateau is one of the most active intracontinental faults worldwide. At least 16 strong earthquakes (M > 6.5) have occurred on this fault since 1327 CE. To reasonably assess the future seismic hazard of this fault region, it is essential to gain a comprehensive knowledge of the fault kinematics and stress state. In this study, we developed a fine 3D geomechanical model of the Xianshuihe fault and its adjacent area, and obtained a spatially continuous contemporary kinematics and crustal background stress field of this region. Our modeled results show that the slip rate of the Xianshuihe fault is as high as 11 mm/a on the northwestern segment and generally decreases to ~9 mm/a on the southeastern segment (i.e. Moxi fault). The Yulongxi fault, a branch oblique to the Moxi fault, has different slip senses in different segments with a very low horizontal slip rate (<0.6 mm/a). In terms of stress, the study area is dominated by a transtensional faulting stress regime with *E*-W-trending maximum horizontal stress S_H, indicating the study area is mainly subjected to an E-W compression and N-S extension. Localized normal and thrust faulting regimes appear alternately along the Xianshuihe fault, showing an inhomogeneous stress state. The high normal stresses on the Songlinkou-Selaha segment and the Moxi fault combined with their relatively high slip rates, make us speculate that these two segments have the potential to produce strong earthquakes in the future. A relatively high seismic hazard is also ascribed to the Yulongxi fault based on the analysis of its geological and geodynamic environment.

1. Introduction

The Xianshuihe fault on the southeastern margin of the Tibetan Plateau is one of the most active intracontinental faults in the world (Fig. 1) (Allen et al., 1991). Geological and geodetic investigations show that this fault is a left-lateral strike-slip fault moving at a high rate of 10–20 mm/a (Allen et al., 1991; Bai et al., 2018; Bai et al., 2021; Gan et al., 2007; Shen et al., 2005), leading to frequent large earthquakes in this area. Since the year 1327, over 16 strong earthquakes of M > 6.5 have been recorded on different segments of the Xianshuihe fault (see Fig. 1), and 8 of these earthquakes reach a magnitude larger than 7.0 (Wen et al., 2008). The latest moderately strong earthquakes are the Kangding M_S 6.3 and M_S 5.8 earthquakes that occurred in 2014, and caused 5 deaths and a direct economic loss of approximately 700 million US dollars (Fang et al., 2015). However, some studies suggested that these two earthquakes did not fully release the energy accumulated in the focal area (Bai et al., 2018; Jiang et al., 2015), and a strong earthquake with a magnitude of M_W 7.0 is still highly possible to strike the Kangding area (Bai et al., 2021).

In recent years, the great area of the Xianshuihe fault has witnessed an increasing number of key infrastructures being constructed, e.g., hydropower stations and the Sichuan-Tibet railway (Fig. 1), accompanied by a growing population. The increased human activities and properties greatly enhanced the demand for seismic hazard assessment for the Xianshuihe fault and its neighboring area. Seismic hazard of a region is often assessed based on knowledge of kinematics and stress

* Corresponding author at: Department of Earth and Space Sciences, Southern University of Science and Technology, Shenzhen 518055, Guangdong, China.
E-mail address: gaok@sustech.edu.cn (K. Gao).

https://doi.org/10.1016/j.tecto.2022.229546
Received 20 March 2022; Received in revised form 30 July 2022; Accepted 6 August 2022
Available online 17 August 2022

state of dominating faults. Fault slip rates are commonly used to investigate the seismic activities of faults and to calculate the recurrence time of potentially damaging earthquakes; the distribution characteristics of stress along a fault plane can be used to directly outline high-stress zones, and provide useful information on the potential hypocenter area of future large earthquakes. Past studies have mainly focused on using fault slip rate (Bai et al., 2018; Bai et al., 2021; Chen et al., 2016; Chevalier et al., 2016) or stress state (Papadimitriou et al., 2004; Parsons et al., 2008; Shan et al., 2013; Toda et al., 2008) to assess the seismic hazard. For example, by using offset geomorphic features near Kangding with ^{10}Be age date, Bai et al. (2021) obtained a Quaternary horizontal slip rate of 8–13.4 mm/a on the southeastern segment of the Xianshuihe fault and suggested that a high seismic hazard with an M_W 7.0 earthquake exists on that segment, especially near the Kangding city. Papadimitriou et al. (2004) and Shan et al. (2013) calculated the changes of Coulomb Failure Stress (ΔCFS) on the Xianshuihe fault caused by

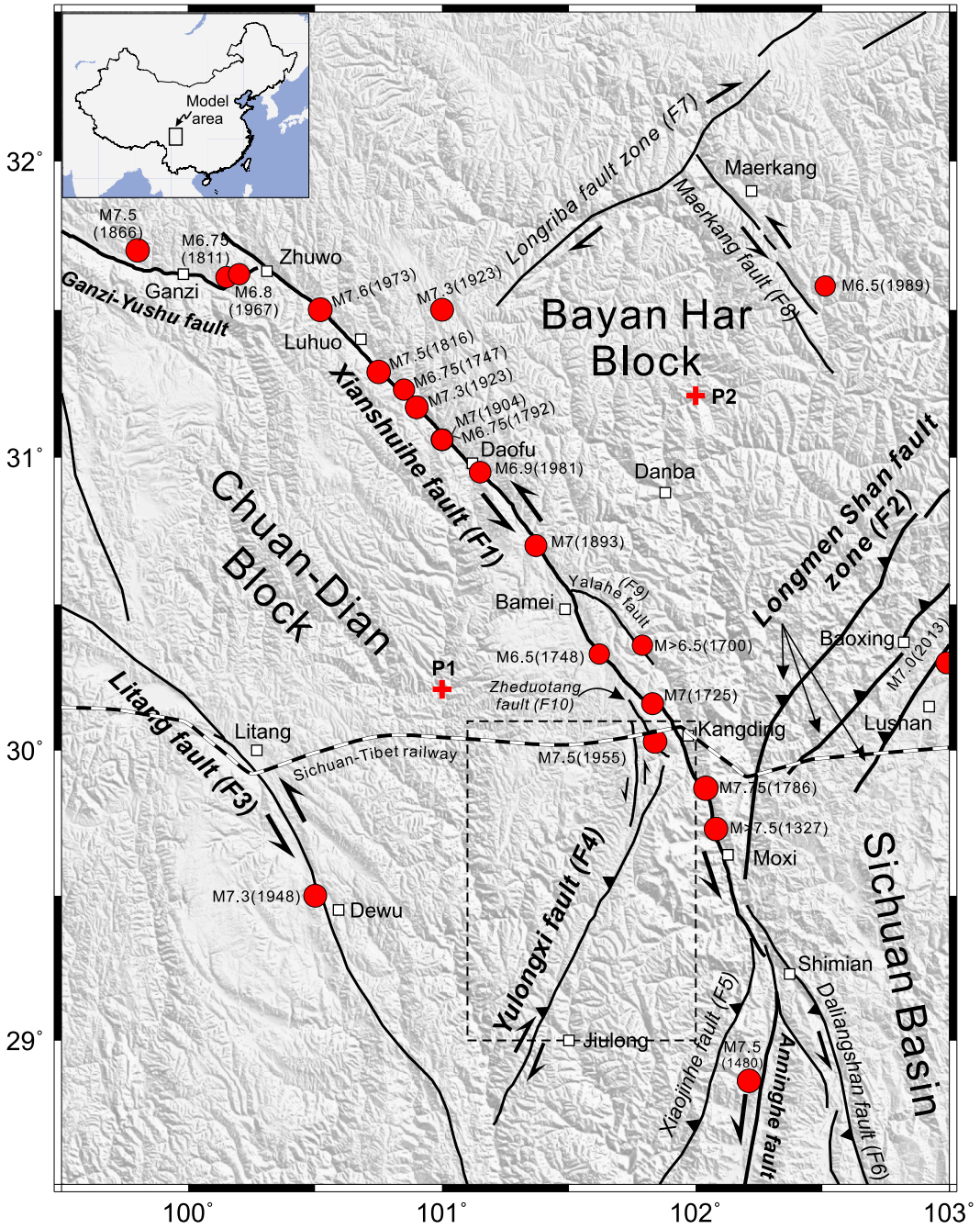

Fig. 1. Map of active faults, earthquakes, and stress measurements in the study area. Fault traces are modified from Deng et al. (2003), Taylor and Yin (2009), Xu et al. (2005), and the China Seismic Experimental Site (CSES, www.cses.ac.cn); stress measurements are from World Stress Map (WSM) (Heidbach et al., 2018); historical earthquake data are from Wen et al. (2008) and the National Earthquake Data Center (https://data.earthquake.cn/). F1-Xianshuihe fault, F2-Longmen Shan fault zone, F3-Litang fault, F4-Yulongxi fault, F5-Xiaojinhe fault, F6-Daliangshan fault, F7-Longriqu fault, F8-Maerkang fault, F9-Yalahe fault, F10-Zheduotang fault. The inset shows the tectonic setting of the Tibetan Plateau; white arrows denote the kinematical pattern of the Tibetan Plateau; the box represents the location of the study area. The red crosses (P1, P2) indicate the locations of two test sites for the comparison with the numerical model shown in Fig. 4b. The dashed box represents the location of Fig. 11. This is also a map of the model region. (For interpretation of the references to colour in this figure legend, the reader is referred to the web version of this article.)

historical earthquakes and suggested that in general, the southeastern segment of the Xianshuihe fault has a high seismic hazard due to the positive ΔCFS.

However, using only kinematic or ΔCFS analysis may fail to give a reliable assessment of a fault's seismic hazard. For example, before the 2008 Wenchuan M_S 8.0 earthquake, the Longmen Shan fault zone was assigned to have a moderate-to-low seismic hazard due to its low slip rate of 1–2 mm/a (Zhang et al., 1999). ΔCFS can only identify faults moving toward or away from failure, and using it solely to evaluate the potential of future earthquakes is known to have great uncertainty as the absolute level of crustal stress is generally unavailable (Toda et al., 2008). An important lesson learned from the Wenchuan M_S 8.0 earthquake is that enhancing seismic hazard evaluation requires multi-source information about a fault from comprehensive observations (Zhang, 2013). However, so far the seismic hazard assessment for the Xianshuihe area has been conducted mostly based on a single information source, such as fault slip rate (Bai et al., 2018; Bai et al., 2021), ΔCFS (e.g., Shan et al., 2013), or historical seismic activity (Wen et al., 2008). Little attention has been paid to combining these information sources to give a comprehensive seismic hazard assessment. In addition, the sparse pointwise information on the fault slip rates (Bai et al., 2018; Bai et al., 2021; Chen et al., 2016) and stress measurements (Hu et al., 2017) distributed on the Xianshuihe fault also limits the reasonable seismic hazard assessment.

To improve the seismic hazard assessment, spatially continuous kinematics and stress information of the Xianshuihe fault is required. Fortunately, numerical modeling is such a powerful tool that can obtain the kinematics and stress of large regions simultaneously. In our previous study (Li et al., 2021, 2022), a large-scale 3D geomechanical model that covers the eastern Tibetan Plateau was established. Based on the first-order features of these simulations, we have identified that the southeastern segment of the Xianshuihe fault has a stress environment that can generate large earthquakes. However, the geometry of the Xianshuihe fault implemented in the model was simplified as one almost vertical surface, and other secondary faults in/near the fault zone were ignored due to its low resolution. To test the inference of the seismic hazard on the southeastern segment of the Xianshuihe fault, a refined model that specifically focuses on the Xianshuihe fault and its adjacent area is needed. The detailed fault data of the SE Tibetan Plateau recently publicized by the China Seismic Experimental Site (CSES) (Lu, 2019) provide a solid foundation for such refined modeling.

In this paper, we construct a more detailed three-dimensional (3D) geomechanical model including the latest geometric data of the fault system, inhomogeneous rock properties, tectonic forces, and gravity for the Xianshuihe fault and its adjacent area. A higher resolution spatially continuous kinematics and stress state of the study area is obtained and calibrated by comparison with model-independent data. Finally, based on the calibrated model results, we synthetically analyze the seismic hazard in the study area. The geological background and model setup of the study area is presented in Section 2. The modeled results and discussion of the seismic hazard potential in the study area are given in Sections 3 and 4, respectively. The conclusions are drawn in Section 5.

2. Geological background and model setup

The study area is located on the southeastern margin of the Tibetan Plateau, where active faults are extensively developed (Fig. 1). As the most important fault in the study area, the Xianshuihe fault plays a key role in understanding the tectonic evolution of the SE Tibetan Plateau. This mainly NW-SE-trending fault has a total length of about 350 km with a clockwise rotation of about 25° in the strike from northwest to southeast (Bai et al., 2021) (Fig. 1). Deep seismic sounding results show that the Xianshuihe fault offsets the Moho in the deep (Wang et al., 2003) and can be treated as a lithospheric-scale block boundary fault. It divides the Songpan-Ganzi terrane (Yin and Harrison, 2000) into the Bayan Har block to the northeast and the Chuan-Dian block to the southwest. Under the continuous southeastward movement of the SE Tibetan Plateau, the Chuan-Dian block moves faster than the Bayan Har block due to the obstruction of the rigid Sichuan basin. This tectonic environment and crustal kinematics make the Xianshuihe fault a large-scale left-lateral strike-slip fault to accommodate the different movement rates between the Chuan-Dian block and the Bayan Har block. As the eastern margin of the Tibetan Plateau, the Longmen Shan fault zone (F2), which is generally a thrust fault zone, separates the Bayan Har block from the South China terrane (Sichuan basin). Large earthquakes on these two block boundary faults (Fig. 1) imply that the current fault activity in the study area is very high and an accurate seismic hazard assessment is thus necessary, especially considering the construction of the Sichuan-Tibet railway crossing the Xianshuihe fault in the Kangding area (see Fig. 1).

Fig. 2 shows an overview of the model setup and workflow adopted in this study. In general, the workflow involves five steps. In the beginning, a geometry model with a more realistic 3D fault system and crustal interfaces is constructed based on thorough geological and geophysical investigations, then the geometry model is discretized into finite elements. In this step, material properties were assigned to the finite element model. Gravity and a pre-stress are also applied to the model volume. Constrained by an appropriate displacement boundary condition, the finite element model is subsequently calculated by the commercial software Abaqus™. After obtaining the results, model-independent data are used to calibrate the modeled results until a good fit between them is reached. Finally, we analyze the modeled results and discuss their implications on the seismic hazard. More detailed information about the model setup is presented below.

2.1. Model geometry

The dimensions of the model are approximately 433 km (99.5°E–103°E) from north to south, 348 km (28.5°–32.5°N) from east to west, and about 70 km thick (Fig. 3). From top to bottom, the model contains a relief of topography and interfaces of the upper, middle, and lower crust. The topology of the surface and the inner-crust interfaces are taken from the GTOPO30 global digital elevation model (USGS) and CRUST1.0 model (Laske et al., 2013), respectively.

The model also includes a complex 3D fault system (see Fig. 3). Some of these fault geometries are determined from the latest China Seismic Experimental Site (CSES, http://www.cses.ac.cn/) fault database, which is compiled from extensive geological and geophysical data (Lu, 2019), such as the Xianshuihe fault (F1), the Litang fault (F3), the Xiaojinhe fault (F5) and the Daliangshan fault (F6). Other faults, including the Longmen Shan fault zone (F2), the Maerkang fault (F8) and the Longriqu fault (F7), are after our previous model (Li et al., 2021). Constrained by earthquake relocation results (Li et al., 2020), the Yalahe fault (F9) and Zheduotang fault (F10) are modeled as dipping toward each other and forming a flower shape together with the Xianshuihe fault. The dip direction of the Yulongxi fault (F4) is still under debate. Magnetotelluric inversion results show that the Yulongxi fault is SE-dipping with a high angle (Jiang et al., 2019), while both the geological map at 1:200,000 scale (Fig. S1) and field investigations (Huang et al., 2000) demonstrate that the fault dips toward NW. Furthermore, field investigations also show that the old Triassic rock on the NW sidewall thrust over the young Cenozoic rock on the SE sidewall. Since only the NW-dipping fault can produce this contact relation, in this model we portray the Yulongxi fault as an NW-dipping fault with an angle of ~65° following previous geological investigations (Huang et al., 2000; Ma, 2013). The Xianshuihe fault is a lithospheric-scale fault (Wang et al., 2003) and is thus set to extend to the bottom of the model (~65 km), while all the remaining faults are crustal-scale faults and are set to terminate at the bottom of the upper crust (~20 km). Table 1 summarizes the geometric characteristics of faults implemented in our model.

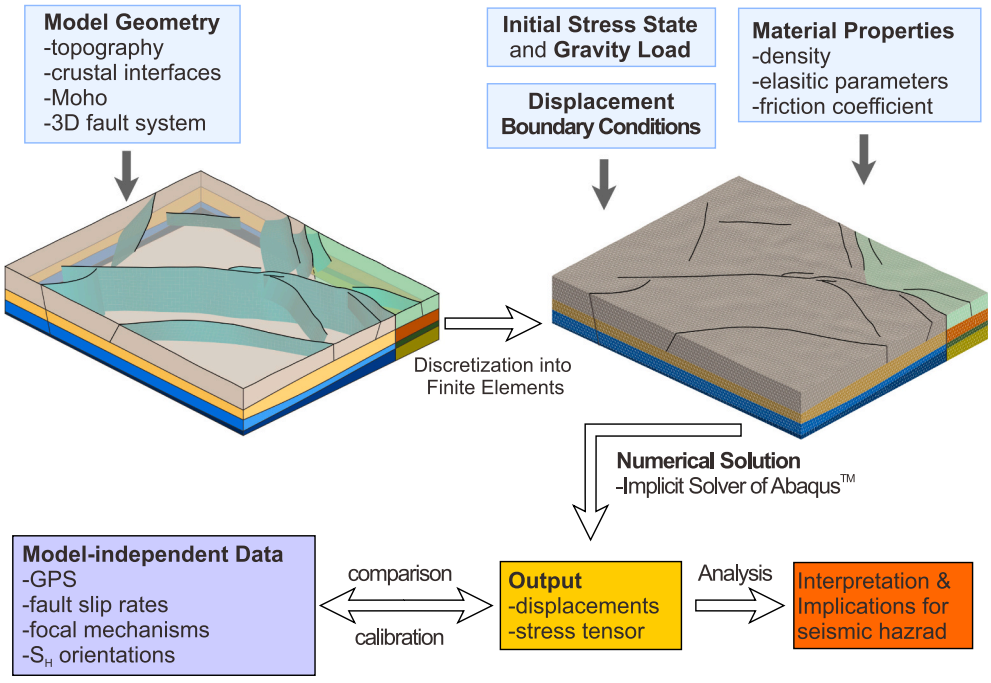

Fig. 2. Model setup and workflow of the geomechanical modeling (modified from Hergert et al., 2015).

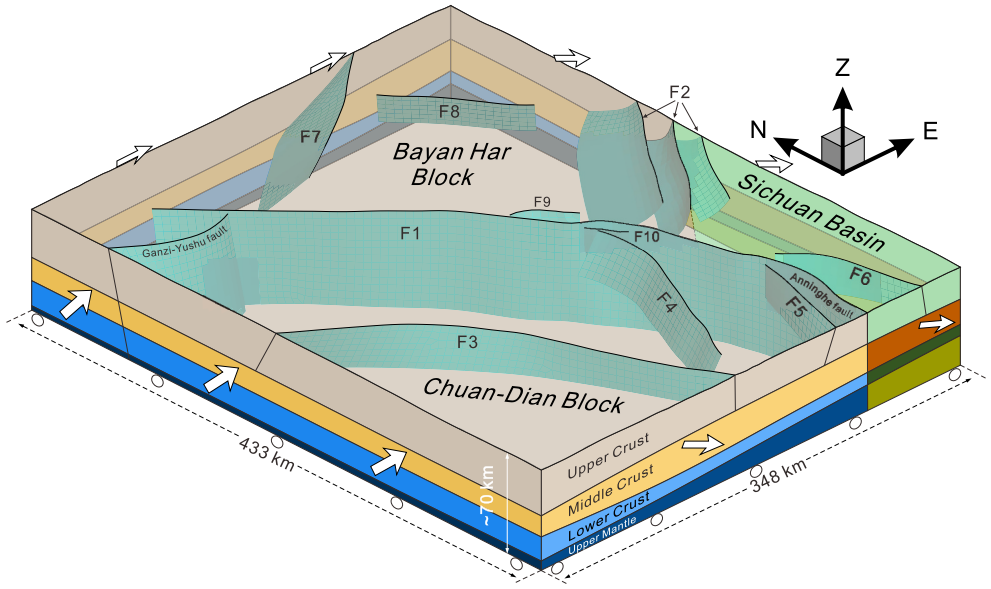

Fig. 3. Geometry of the implemented fault system in the 3D geomechanical numerical model. Different layer colors refer to different rock properties. The white arrows and circles denote the boundary condition settings of the model.

2.2. Rock properties

In the model, the properties of rocks are assumed to be linear and static elasticity, which are converted from the P wave velocity using empirical relations (Brocher, 2005; Brotons et al., 2016). Although rocks are not elastic throughout the entire crustal depth, previous studies about the evolution of large faults show that the continental lithosphere has a long-term elasticity and exhibits elastic-brittle behavior in millions of years (Armijo et al., 2004; Hubert-Ferrari et al., 2003). The study area includes the South China terrane and the Songpan-Ganzi terrane. Table 2 summarizes the material parameters used in the model.

The faults considered in the model are simplified as pairs of contact surfaces that can slide with each other and are constrained by the Mohr-Coulomb friction law. The effective friction coefficient of all faults is set as 0.06, which is the best value for the minimum misfit between the measured velocities at the surface and the modeled kinematic results (see Fig. 4a). This value is also consistent with the <0.08 effective friction coefficient suggested by He and Lu (2007) for the Xianshuihe fault.

2.3. Initial stress state

The initial stress state of the model refers to the force that the model contains to balance with gravity when it is not subjected to any horizontal tectonic forces. We use the calculation formula proposed by Sheorey (1994) to determine the initial crustal stress, i.e.,

Table 1
Geometry of the faults implemented in the model.

No.	Fault name	Dip direction/Dip (°)	Reference
F1	Xianshuihe F.	−/90	Lu (2019)
F2	Longmen Shan F.	NW/50 (listric)	Li et al. (2021)
F3	Litang F.	North: NE/70 Middle: SW/80 South: NE/85	Lu (2019)
F4	Yulongxi F.	NW/65	Huang et al. (2000); Ma (2013)
F5	Xiaojinhe F.	NW/60	Lu (2019)
F6	Daliangshan F.	−/90	Lu (2019)
F7	Longriba F.	NW/45	Lu (2019)
F8	Maerkang F.	NE/60	Gong et al. (1995)
F9	Yalahe F.	SW/80	Li et al. (2020)
F10	Zheduotang F.	NE/75	Li et al. (2020)

Note: the geometries of faults F1, F3, F5–7 is reconstructed from the scattered 3D point data.

Table 2
Elastic parameters and densities in the 3D geomechanical model.

Layers	South China terrane (Sichuan basin)			Songpan-Ganzi terrane (Bayan Har block, Chuan-Dian block)		
	E (GPa)	ρ (g/cm^3)	ν	E (GPa)	ρ (g/cm^3)	ν
Upper crust	78.57	2.74	0.25	75.29	2.72	0.25
Middle crust	87.31	2.80	0.25	81.97	2.76	0.25
Lower crust	110.04	2.94	0.25	89.16	2.81	0.25
Upper mantle	199.25	3.34	0.28	174.72	3.26	0.28

E, ρ and ν denote Young's modulus, density, and Poisson's ratio, respectively.

$$k = 0.25 + 7E(0.001 + 1/z) \quad (1)$$

where k is the ratio between mean horizontal stress and vertical stress, E is Young's modulus (GPa), and z is the burial depth (m). This analytical initial stress state has been widely used in crustal stress studies in Germany (Ahlers et al., 2021), Canada (Reiter and Heidbach, 2014), and Turkey (Hergert and Heidbach, 2011), and achieved good results. The comparison in Fig. 4b shows a good consistency between the k value predicted by Eq. (1) and the modeled k value at two test sites that are far away from the faults and model boundaries (see Fig. 1).

2.4. Kinematic boundary conditions

For the kinematic boundary conditions, we used the Global Position System (GPS) data obtained by Wang and Shen (2020) and Wang et al. (2017) to drive the horizontal movement of the model and simulate the tectonic loadings (Fig. 5). The velocities at nodes located on the boundary of the model are interpolated from the GPS observations (see the black arrows in Fig. 5). The model bottom is vertically fixed but horizontally movable (see Fig. 3). The model surface is free to move. To compare with the GPS-derived velocities, the faults are set to be locked in the upper crust to represent the interseismic velocities. The model time is set to be 200 ka to allow the accumulated displacements at the boundaries to propagate into the model thus generating a proper contemporary state of stress and deformation.

Finally, the volume of the 3D model is discretized into ~4 million linear tetrahedral elements. The element size is 1–2 km on the faults and ~5 km near the model boundaries. We used the commercial finite element software Abaqus™ for the calculation. The modeled displacement and stress results are compared and calibrated with the model-independent data, such as the GPS observations, fault slip rates, focal mechanism solutions, and S_H orientations. Finally, we obtain a 3D geomechanical model that can well match the kinematic and dynamic observations in the study area.

3. Results

3.1. Crustal horizontal velocities and fault slip rates

As mentioned in Section 2.4, in the beginning, the faults in the upper crust are set to be locked with an infinite effective friction coefficient. After a good fit between the modeled velocities and GPS measurements is achieved, the faults are changed to be unlocked with a low effective coefficient of friction, then the same boundary conditions as in Fig. 5 are imposed to finally obtain the long-term kinematics and stress evolution. We then compare the modeled results with model-independent data in terms of kinematics and stress field. For the kinematics, the surface motion rates and fault slip rates are extracted from the model to compare with GPS measurements and geological fault slip rates, respectively. For the stress field, the simulated maximum horizontal stress azimuth S_H is compared with the data from the World Stress Map (WSM), and the modeled stress regime is compared with the regime revealed by the focal mechanism solution. These comparisons allow us to evaluate the accuracy of the modeled results and hence ensure the reliability of subsequent seismic hazard analyses.

Fig. 6a presents the results of horizontal crustal movement in the study area. In general, the crust moves southeastward. Taking the Xianshuihe fault as a boundary, the study area involves two distinct kinematic patterns: the slow Bayan Har block on the northeast side and

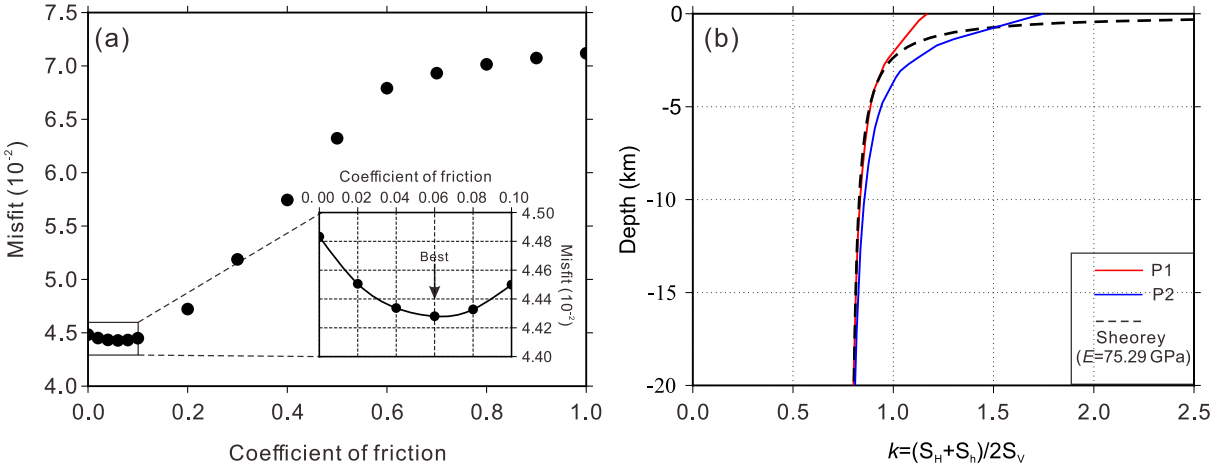

Fig. 4. (a) Crustal velocity misfits between the modeled results and GPS measurements when using different effective friction coefficients. The value 0.06 is selected as the best friction coefficient. The GPS measurements within ~5 km of faults are excluded in the calculation. (b) Comparison of the initial k values at two test sites (P1 and P2) with the theoretical curve (black dashed line) proposed by Sheorey (1994). The locations of P1 and P2 are given in Fig. 1.

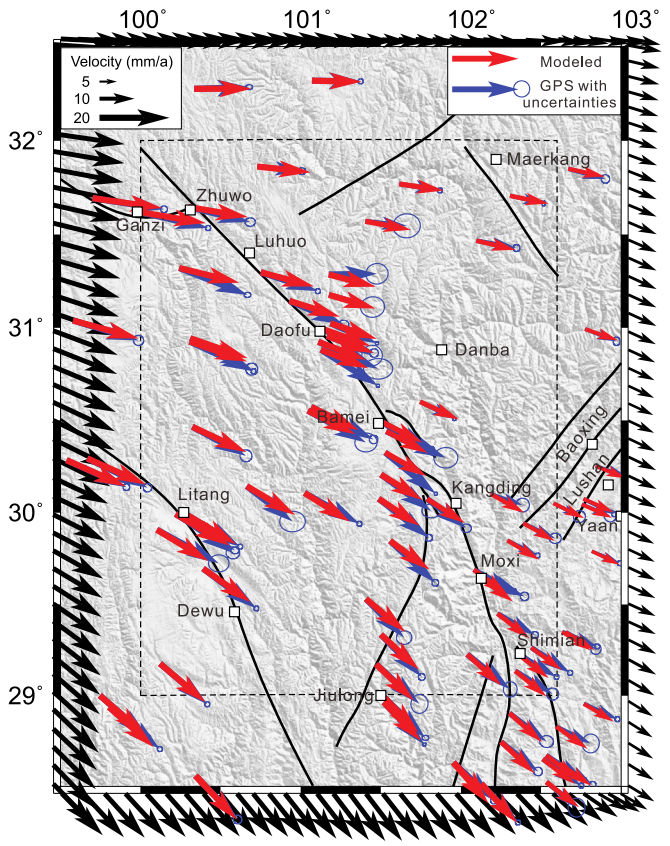

Fig. 5. Setting of boundary conditions applied on the model and comparison between the GPS observations and our modeled horizontal velocities. The black, red, and blue arrows represent the lateral boundary movements, the modeled velocities at the surface, and the GPS measurements, respectively. The black dashed line represents the main area of interest, to which the model boundary shrinks inward by approximately 50 km to reduce possible boundary effects. (For interpretation of the references to colour in this figure legend, the reader is referred to the web version of this article.)

the fast Chuan-Dian block on the southwest side. The movement rate of the Chuan-Dian block decreases from ~21 mm/a in the north to ~16–17 mm/a in the south, and it is much higher than that of the corresponding locations in the Bayan Har block, which is ~16 mm/a in the northwest corner of the model and gradually decreases to 9–10 mm/a toward the southeast. The obvious rate difference between the Chuan-Dian block and the Bayan Har block leads to a high left-lateral slip rate of the Xianshuihe fault.

Fig. 6b shows the distribution of modeled fault slip rate in the study area. The maximum slip rate on the Xianshuihe fault is about 10–11 mm/a, which is located in the Luhuo-Daofu-Bamei segment. As the fault terminates northwestward in the west of Zhuwo, the slip rate on the fault also decreases to ~2 mm/a correspondingly. To the southeast, the slip rate gradually decreases from 10–11 mm/a to 6–7 mm/a in Shimian. Nearly parallel to the Xianshuihe fault, the left-lateral Litang fault slips at 2.2–2.4 mm/a on the northwestern segment and decreases to 1.2–1.4 mm/a toward the southeast. The horizontal slip rate on the Yulongxi fault (F4) is as low as <0.7 mm/a since it intersects with the direction of crustal movement at a high angle. The modeled sense of slip on the Yulongxi fault is not uniform along its strike. The northeastern segment is left-lateral while the southwestern segment is right-lateral. The slip rates on the Yalahe (F9) and Zheduotang (F10) branches are both low (<1.2–1.4 mm/a).

The comparison in Fig. 5 shows that the modeled crustal velocities in most places have good agreement with the GPS measurements except for a few individual sites. In addition, we also collect the long-term slip rates obtained based on geological methods in the study area (Table 3) and plot them in Fig. 6b. The geological slip rate of the northwestern segment of the Xianshuihe fault is 15 ± 5 mm/a (Allen et al., 1991), and gradually decreases to ~9 mm/a in the southeastern segment (Chen et al., 2016; Yan and Lin, 2017), which is consistent with our simulated fault slip rate. However, our results seem to be contradictory to the investigations in Bai et al. (2018, 2021), in which the long-term slip rate of the Xianshuihe fault increases from northwest to southeast. Bai et al. (2021) suggested that this increasing trend in slip rate is caused by the decreased eastward movement rate of the Bayan Har block, which is the result of the obstruction of the rigid Sichuan basin. However, our simulation indicates that the rate of the southeastward movement of the Chuan-Dian block also gradually decreases (Fig. 6a). Therefore, it is difficult to conclude that the slip rate of the Xianshuihe fault increases toward the southeast. In fact, the southeastern segment of the Xianshuihe fault, namely the Moxi fault, is under strong lateral compression and in a transpressional environment, which is not only shown by our modeled results (Fig. 7b), but also evident from the widespread thrust faults and folds, as well as the thrust faulting focal mechanism solutions in the east of the Moxi fault (Fig. 7b). Physically, high normal stress means high friction and makes the fault more difficult to slip. Therefore, we consider that the slip rate of the Moxi fault should be lower than that on the northwestern segment of the Xianshuihe fault. The slip deficit on the Moxi fault is inferred to be converted into the uplift of the Gongga Mountain (Xu et al., 2003; Tan et al., 2010). For the Litang fault, although our simulated 2.0–2.4 mm/a fault slip rate is lower than the ~4 mm/a slip rate shown in Xu et al. (2005), it is approximate to the ~2 mm/a reported by Chevalier et al. (2016). The slip rate of the Yulongxi fault revealed by our model is as low as <0.7 mm/a, and the sense of fault slip is different in different segments. These features are inconsistent with the 3 ± 0.3 mm/a left-lateral strike-slip rate obtained in Chen et al. (2016) but are well consistent with the field observations of Huang et al. (2000) and Zhang et al. (2011). Future fieldwork on the long-term slip rate and slip sense of this fault should therefore be conducted carefully. For the Longriba fault zone and the Longmen Shan fault zone, only a small part of them is included in our model. More detailed comparsion of the modeled slip rates with those determined by geological methods for these two faults is referred to Li et al. (2021), which indicates good consistency between them.

3.2. *Stress orientation and stress regime*

To investigate the stress state in the study area, we extract stress tensors at the 5 km depth below sea level (BSL) from the numerical model. This selected depth for slicing the model is the average depth of earthquakes in this area when the ~5 km average altitude is considered. The orientation of the maximum horizontal stress (S_H) is calculated according to the method of Lund and Townend (2007).

Fig. 7a shows that the S_H in the study area is generally in the E-W direction. Near the Xianshuihe fault, the S_H orientation changes significantly, deflecting from near E-W to nearly perpendicular or nearly parallel to the fault strike. On the Bamei-Kangding segment in the middle of the Xianshuihe fault, the S_H orientation changes drastically, forming a local circle S_H trajectory (Fig. 7a), which is thought to be due to the complex fault system in this segment and its vicinity. In this area, the Xianshuihe fault is split into three branches, i.e., the Yalahe fault (F9), the Selaha fault segment and the Zheduotang fault (F10), and an obvious releasing bend (Mugecuo bend) is developed on the Selaha fault (Fig. 7b). In addition, both the northern end of the Yulongxi fault and the southwestern end of the Longmen Shan fault zone are also terminated in this area (Fig. 1). These complex fault geometries and the intersection of multiple faults play a key role in the formation of dramatic changes in the stress orientation at this location.

The modeled stress regime at the 5 km depth BSL in the study area is visualized by the Regime Stress Ratio (RSR) (Simpson, 1997) (Fig. 7b). Overall, the study area is dominated by a strike-slip faulting stress

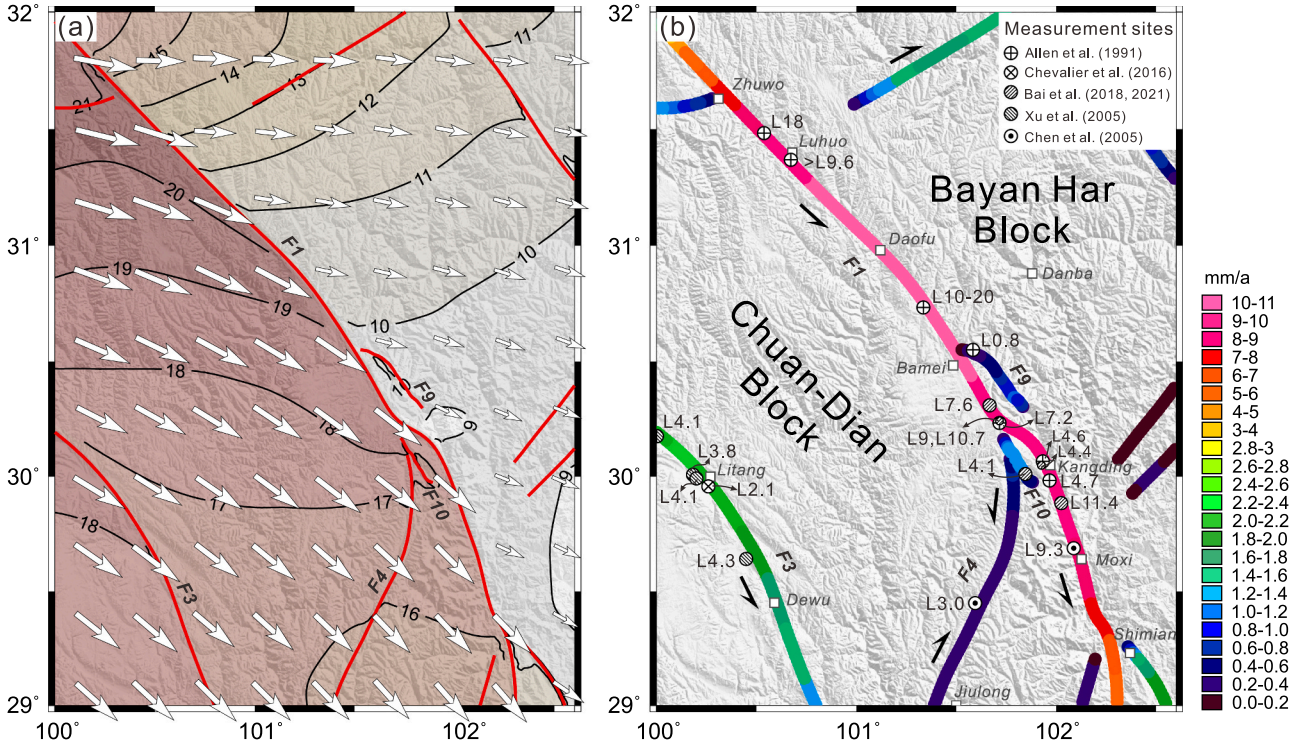

Fig. 6. (a) The modeled crustal surface velocities in the study area. White arrows indicate the movement direction of the crust. The background colour contours and the corresponding labels denote the magnitude of the velocity (in mm/a). The red lines show the faults considered in the model. (b) The comparison between our modeled horizontal fault slip rates with previous studies. The half arrows show the modeled fault slip senses. The numbers after "L" are fault slip rates from previous studies. The Letter "L" denotes Left-lateral slip. (For interpretation of the references to colour in this figure legend, the reader is referred to the web version of this article.)

regime. The northern part of the Bayan Har block is dominated by transpression, while the southern part of the Bayan Har block and the Sichuan-Yunnan block are dominated by transtension. Obvious variations of stress regime are observed along faults. For example, on the Xianshuihe fault, the Zhuwo-Luhuo-Daofu segment and north of Kangding are in a normal faulting stress regime, while Bamei and Moxi segments are in a thrust faulting stress regime.

The comparison in Fig. 7a shows that our modeling results are in good agreement with the WSM data of quality A–C. The average angle difference between the two is about 27° and is only slightly higher than the ±25° error of S_H orientation derived from focal mechanism solutions (Heidbach et al., 2018). We have also collected the focal mechanism solutions of earthquakes located in the study area from previously published literature and datasets and classified them into normal, strike-slip, thrust, and mixed-type events in terms of the tectonic regime (Zoback, 1992) (Fig. 7b). Based on the earthquake focal mechanism solutions, the dominant stress regime in the study area is revealed to be strike-slip to normal faulting. Comparing our modeled stress regime and the earthquake type revealed by the focal mechanism solutions shows that the two are roughly in agreement. Although the local modeled normal or thrust faulting stress regimes along the Xianshuihe fault seem to conflict with the strike-slip motion of this fault, it should be noted that the RSR value only describes the slip pattern of an optimally oriented fault in the given stress field. The near-vertical Xianshuihe fault is not optimally oriented in the stress field, thus the discrepancy between our modeled stress regime and the fault kinematics is reasonable.

3.3. Stress states along important faults

In this study, the normal stress distribution on the fault surface is derived from the modeled stress tensors. Higher normal stress hinders fault sliding, and can thus accumulate higher strain energy to produce large earthquakes. On the contrary, lower normal stress is conducive to fault sliding, allowing it to release energy in time, thereby having less potential to incubate large earthquakes.

3.3.1. The Xianshuihe fault

Fig. 8a shows the modeled normal stress on the Xianshuihe fault surface above the depth of 20 km BSL, which approximately corresponds to the thickness of the seismic layer in this area (Fang et al., 2015). The fault normal stress increases downward with considerable lateral changes (Fig. 8a). Roughly bounded by Songlinkou, the Xianshuihe fault can be divided into the northwestern segment (Zhuwo-Songlinkou) and the southeastern segment (Songlinkou-Shimian). The normal stress on the northwestern segment is significantly lower than that on the southeastern one. For example, at the 10 km depth BSL, the normal stress on the northwestern segment is about 100–300 MPa, much lower than the 400–600 MPa on the southeastern segment. Two releasing bends, i.e., the Mugecuo bend and the relatively small bend near Shimian on the southeastern segment, with significantly low normal stress, are also revealed in Fig. 8. These relatively higher and lower normal stresses on the fault surface are in line with the local stress regimes in which the corresponding fault segments are located. For example, the northwestern segment has lower normal stress, and it is also dominated by a normal faulting stress regime; the fault normal stress increases significantly on the southeastern segment where a predominated thrusting stress regime can be observed (see Fig. 7b).

3.3.2. The Litang fault and the Yulongxi fault

Fig. 8b and c show the normal stress distribution on the Litang fault and the Yulongxi fault, respectively. Vertically, the normal stress increases with depth. Different from the Xianshuihe fault, the distribution of normal stress on these two faults has a weaker lateral change. This is due to their relatively simple geometry, e.g., no apparent bendings. The

Table 3
Compilation of reported geological fault slip rates and comparison with our modeled results in the study area.

No.	Name	Location (Long. Lat.)		This study (mm/a)	Geological slip rate* (mm/a)	Reference
F1	Xianshuihe F.	100.54	31.48	L9–10	L18	Allen et al. (1991)
		100.67	31.37	L9–10	>L9.6	
		101.34	30.73	L10–11	L10–20	
		101.58	30.55	L0.2–0.4	L0.8	
		101.72	30.23	L9–10	L7.2	
		101.93	30.07	L9–10	L4.6	
		101.97	29.98	L9–10	L4.7	
		101.67	30.31	L9–10	L7.6(+2.3/−1.9)	Bai et al. (2018, 2021)
		101.72	30.24	L9–10	L9(+1.1/−0.9), L10.7 (+1.3/−1.1)	
		101.93	30.05	L9–10	L4.4 ± 0.5	
		101.85	30.00	L0.6–0.8	L4.1 ± 0.7	
		102.01	29.88	L9–10	L11.4 (+2.0/−1.8)	
		102.09	29.69	L8–9	L9.3 ± 1.0	Chen et al. (2016)
F3	Litang F.	99.54	30.48	–	L2.3 ± 0.6	Chevalier et al. (2016)
		100.26	29.96	L2.0–2.2	L2.1 ± 0.2	
		100.00	30.18	L2.0–2.2	L4.1 ± 0.9	Xu et al. (2005)
		100.18	30.01	L2.0–2.2	L3.8 ± 0.8	
		100.20	30.00	L2.0–2.2	L4.1 ± 1.0	
		100.45	29.64	L1.8–2.0	L4.3 ± 1.0	
F4	Yulongxi F.	100.59	29.45	North: L0.2–0.6 South: R0.2–0.4	L3.0 ± 0.3	Chen et al. (2016)

* The letter "L" and "R" in front of the slip rate indicates the left-lateral and right-lateral slip senses, respectively.

normal stress of the northwestern segment of the Litang fault is slightly smaller than that of the southeastern segment, which is consistent with the normal fault stress regime of the northwestern segment (Fig. 7b). On the contrary, the lateral change of normal stress on the Yulongxi fault is not obvious. However, at the same depth, the normal stress value on the Yulongxi fault is notably higher than that of the Litang fault, indicating that the former has suffered from a stronger lateral compression.

4. Discussion

From Bamei to Kangding, the Xianshuihe fault is divided into three branch faults, namely the Yalahe fault, the Selaha fault (the main active branch), and the Zheduotang fault (Fig. 9a). In our previous study (Li et al., 2021, 2022), the first-order modeled results showed that the normal fault stress regime exists in the entire area between Bamei and Kangding, which is attributed to the clockwise rotation of the Xianshuihe fault. In this study, we constructed a smaller but more detailed model focusing on the Xianshuihe fault and its adjacent area using the latest fault geometry data. The new model results show that the extent of the normal faulting stress regime is smaller than that in our previous findings, mainly existing between Salaha and Kangding, and extending eastward to the southwestern end of the Longmen Shan fault zone (Fig. 9a).

4.1. Normal faulting stress regime on the Mugecuo bend

The Selaha fault and the Moxi fault in the south form a left-stepping strike-slip fault system and these two faults are linked by the Mugecuo bend located between Seraha and Kangding (Fig. 9a). Due to the left-lateral strike-slip motion of the Xianshuihe fault, the Mugecuo bend appears as a releasing bend, which is consistent with our modeled stress results showing that the Mugecuo bend is dominated by the normal faulting stress regime (RSR < 1) (Fig. 9a). The Sichuan-Tibet railway crosses this segment and is threatened by potential earthquakes on this segment (Bai et al., 2021).

Obviously, this normal fault stress regime is caused by the extension of the Mugecuo bend under the left-lateral strike-slip of the Xianshuihe fault. The Mugecuo lake located on this bend represents a pull-apart basin formed in this tectonic environment (Allen et al., 1991). Bai et al. (2021) suggested that the Mugecuo pull-apart basin was mainly controlled by the SE Selaha fault (southeastern part of the Mugecuo bend) and the Zheduotang fault. However, the kinematic results of our model show that the Zheduotang fault has a very low slip rate (Fig. 6b) and is hard to act as the boundary strike-slip fault for the pull-apart basin. In fact, field investigations suggested that the Zheduotang fault is a transtensional fault dominated by vertical displacement (Zhao, 1987). In addition, it should be noted that the Zheduotang fault and the NW Selaha fault form a right step-over at Selaha (Fig. 9a). Assuming that the Zheduotang fault had a high enough slip rate and could act as a boundary strike-slip fault of the pull-apart basin, the crust in the right step-over would be pushed together by the left-lateral fault slip and should form contractional structures near Selaha. However, this inference contradicts the existed normal secondary faults there (Pan et al., 2020). Therefore, we consider that the Zheduotang fault did not play an important role in the formation of the Mugecuo pull-apart basin, which implies that the slip rate of the Zheduotang fault may not be high. Instead, we consider the boundary strike-slip faults of the Mugecuo pull-apart basin should be the Selaha fault and the Moxi fault.

Fig. 9a shows that the normal faulting stress regime that initiated on the Mugecuo bend extends eastward to the southwestern end of the Longmen Shan fault zone, which was also noted in our previous study (Li et al., 2022). To verify the effect of the Mugecuo releasing bend on the normal faulting stress regime, we further conduct another test model within which the Xianshuihe fault is locked, while other model settings remain unchanged. The test results show that the normal faulting stress regime in the Mugecuo bend and its east disappears (Fig. 9b). Comparing Fig. 9a and b indicates that the normal faulting stress regime is indeed attributed to the slip on the Mugecuo releasing bend and it has already extended to the southwestern end of the Longmen Shan fault zone. The predominant occurrence of normal faulting earthquakes at the southwestern end of the Longmen Shan fault zone (Long and Zhao, 2000) provides direct evidence for our model results.

4.2. Seismic hazard potential of the Xianshuihe fault

Seismic hazard generally describes the potential for a damaging earthquake in a region within a specific period of time (McGuire, 2004; Field and WGCEP, 2018). Seismic hazard analysis can provide information on the location, time and magnitude of a potential earthquake, as well as the associated expectable ground motions (Hergert, 2009), although uncertainties exist in each step of the whole process. Many studies of seismic hazard assessment have been conducted worldwide due to the strong demands from society and the construction of new critical facilities. For example, to obtain a reasonable assessment of seismic hazard in Istanbul (Turkey), threatened by the high activities of the North Anatolian Fault, especially after the occurrence of the 1999 Izmit M_W 7.4 earthquake, Parsons (2004) calculated the time-dependent occurrence probability of earthquakes beneath the Marmara Sea region, in front of Istanbul, by incorporating stress changes caused by the 1999 Izmit M_W 7.4 earthquake and suggested that the probability of having an $M \geq 7$ earthquake is as high as 53 ± 18% in the next 30 years (2004–2034). For California (USA), the third Uniform California Earthquake Rupture Forecast (UCERF3) has been developed by the Working Group on California Earthquake Probabilities (WGCEP) and is thought to be the most advanced model of its kind to date (Field et al., 2015; Field and WGCEP, 2018). The model consists of four main

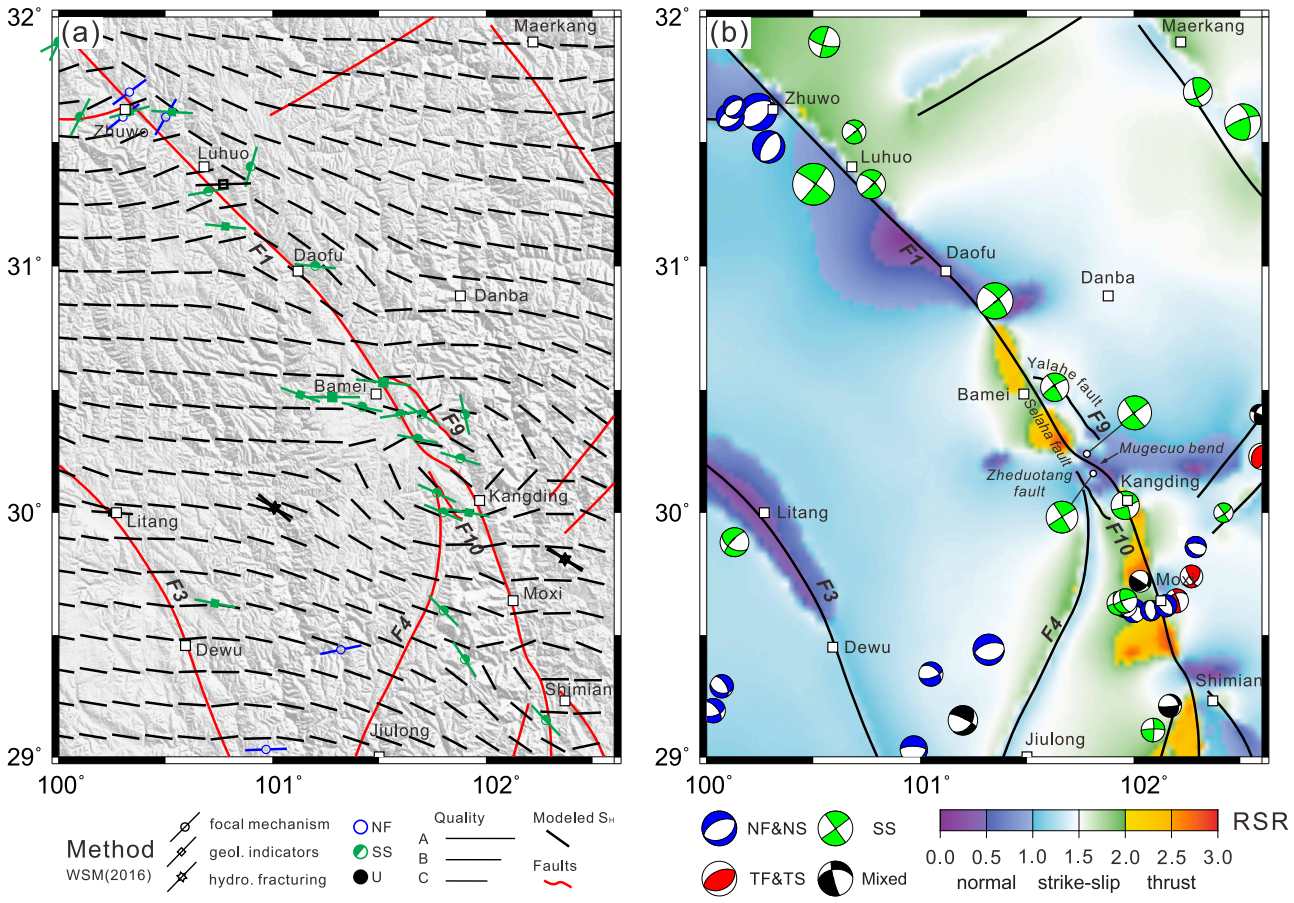

Fig. 7. (a) Modeled S_H orientation at the 5 km depth BSL, with grid space of 15 km × 15 km in longitude and latitude, respectively. Black bars show the modeled S_H orientations. Colored bars show the S_H orientations of quality A–C from the WSM database (Heidbach et al., 2018). Red lines show the fault traces considered in our model. (b) Modeled stress regime at the depth of 5 km BSL in terms of the regime stress ratio (RSR). Focal mechanism solutions are from GCMT (www.globalcmt.org), CSES (China Seismic Experimental Site, www.cses.ac.cn), and published literature (Li et al., 2019; Molnar and Deng, 1984; Molnar and Lyon-Caent, 1989; Wang, 1992). (For interpretation of the references to colour in this figure legend, the reader is referred to the web version of this article.)

components (i.e., fault model, deformation model, earthquake-rate model and probability model) and can provide time-dependent self-consistent estimates of magnitude, location and likelihood of potential earthquakes in the California region (Field et al., 2015). In the framework of the current seismic hazard assessment, fault slip rates and fault geometries as well as segmentation schemes play key roles in calculating the final probabilities of earthquake occurrence (Hergert, 2009), whereas epistemic uncertainties inevitably exist in determining these parameters. To help minimize these uncertainties, this paper provides the spatially continuous fault stress states and long-term slip rates in the southeastern Tibetan Plateau and gives indications for the potential rupture segments in this region in the future.

As mentioned in the Introduction section, many studies have focused on the seismic hazard of the Xianshuihe fault. These studies have used a series of methods including ΔCFS (e.g., Parsons et al., 2008; Shan et al., 2013; Toda et al., 2008), seismic gap analysis (e.g., Wen et al., 2008), geodetic surveys (e.g., Jiang et al., 2015) and long-term fault slip rate (e.g., Bai et al., 2018; Bai et al., 2021) to assess the potential rupture segment in the Xianshuihe fault. Fig. 10 shows a compilation of reported potential rupture segments. It can be seen that all the inferred dangerous segments are located in the southeastern part of the Xianshuihe fault (south of Songlinkou), although different authors prefer different segments.

Most ΔCFS studies suggested that the northern portion of the southeastern part of the Xianshuihe fault has a high seismic hazard, such as the Bamei-Selaha segment (Papadimitriou et al., 2004), the longer Songlinkou-Selaha segment (Shan et al., 2013), or the longest Songlinkou-Kangding segment (Parsons et al., 2008; Toda et al., 2008) (Fig. 10). The difference in length is probably related to the use of different model settings or historical earthquakes in these calculations. For example, in Papadimitriou et al. (2004), the rock property was set as elastic, while Shan et al. (2013) adopted a multi-layered elastic-visco-elastic rock property; Toda et al. (2008) and Parsons et al. (2008) mainly concerned the impact of the 2008 Wenchuan M_S 8.0 earthquake on the Xianshuihe fault located 170 km west of the epicenter and therefore neglected the effects of historical earthquakes in this area. Other studies, such as seismic gap analysis (Wen et al., 2008) and using fault slip deficit inverted from geodetic data (Jiang et al., 2015) respectively identified high seismic hazard on the Bamei-Selaha and Songlinkou-Selaha segments, which are consistent with the results of ΔCFS.

Only a few studies pointed out the segment of the Xianshuihe fault located south of Kangding, namely the Moxi fault, is dangerous. Based on the long-term fault slip rate on the Moxi fault, Bai et al. (2021) assigned an M_W 7.0 earthquake seismic hazard to this segment considering the accumulated fault slip deficit since its last strong earthquake. Consistent with Bai et al. (2021), in our previous work (Li et al., 2021, 2022), the first-order features of the model results showed that the Moxi fault is under stronger compression and has a relatively high slip rate, indicating its high potential to generate strong earthquakes in the future.

Compared with our previous work, the results of this study, in which the geomechanical model is refined with higher resolution and updated fault geometries, show that not only the Kangding-Shimian (Moxi fault) segment but also the Songlinkou-Selaha segment are located in thrust faulting stress regimes and are separated by the normal faulting stress

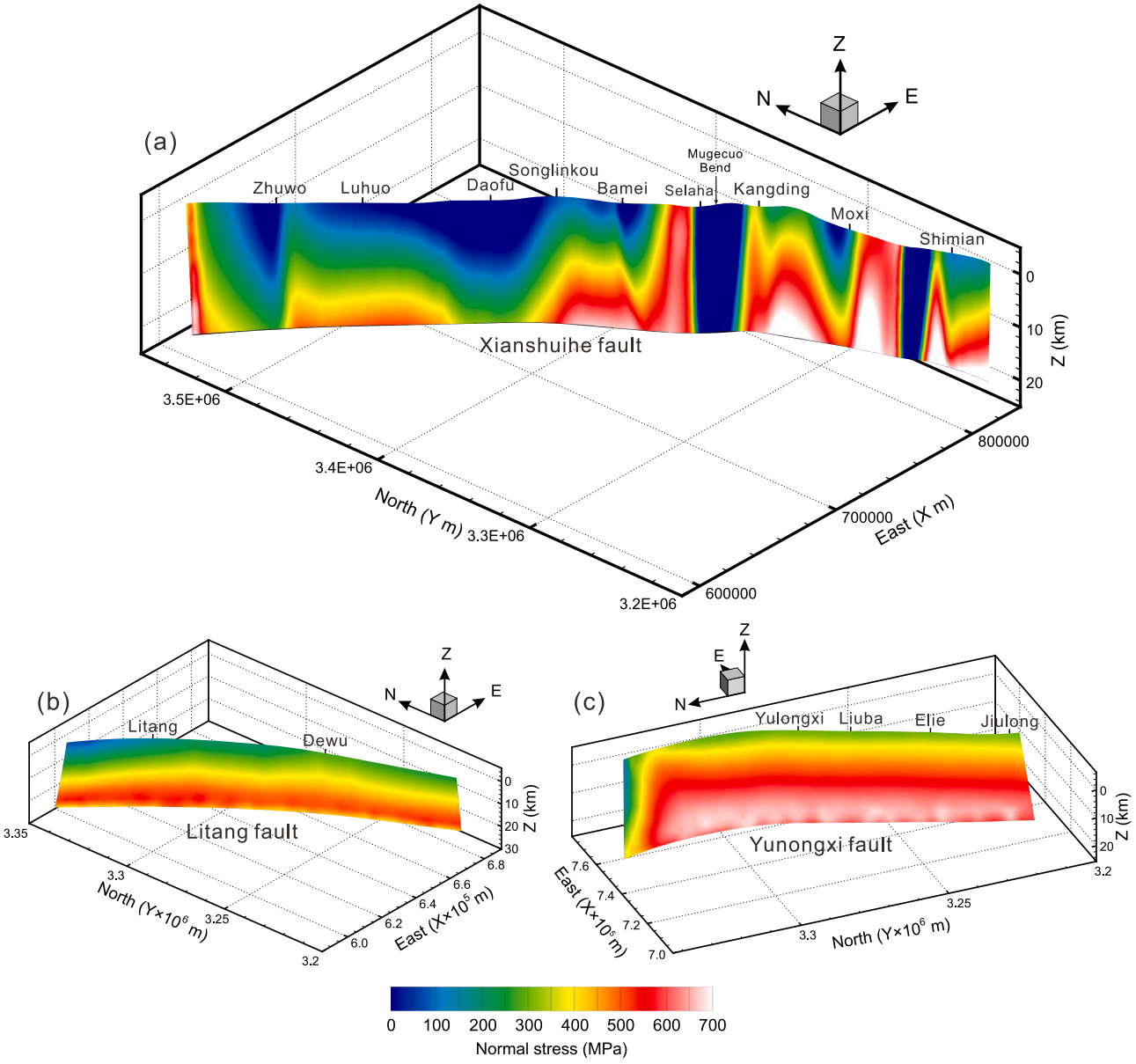

Fig. 8. Distribution of normal stress on (a) the Xianshuihe fault, (b) the Litang fault, and (c) the Yulongxi fault.

regime of the Mugecuo releasing bend (Fig. 10). Due to the two clockwise rotations (~10°, from NW to SE) of the strike of the Xianshuihe fault at Songlinkou and Kangding (see Fig. 7b), the angle between the fault strike and the movement direction of the Chuan-Dian block increases. On a large scale, these changes in the fault strike make the whole southeastern part of the Xianshuihe fault (Songlinkou-Shimian) a large restraining bend that is subjected to the compression from the Chuan-Dian block. Due to this compression, the normal stress on the fault surface of the Songlinkou-Selaha segment and the Moxi fault increases (Fig. 8a) and forms a thrust faulting stress regime in these two segments (Fig. 10). Higher normal stress on a fault means that a stronger friction force needs to be overcome before the fault can slip, and it also means that higher energy can be accumulated on the fault. Once the shear stress reaches the strength of the rock, the accumulated energy will be rapidly released through rock fracture, forming a large earthquake. Therefore, we believe the Songlinkou-Salaha segment and the Moxi fault are of high seismic hazard, especially when considering the high slip rates (~9 mm/a) of these segments (Fig. 6b). Proofs from historical earthquake records and investigations of paleoseismic events on the Moxi fault indicate that its average recurrence interval of strong earthquakes is about 300 years (Yan and Lin, 2017; Zhou et al., 2001). When comparing the time elapsed from the previous 1786 M 7.75 earthquake (236 years) and the average earthquake recurrence interval on this segment, the Moxi fault is approaching rupture and of high seismic hazard. For the Songlinkou-Selaha segment, paleoseismic investigations reveal that five strong earthquakes have occurred during the past 9000 years (Li et al., 2017). This segment has been identified as a seismic gap since no strong earthquakes occur again after the 1893 M 7 earthquake (Qian et al., 1988; Allen et al., 1991; Wen et al., 2008), and the energy accumulated in this fault segment is capable to produce an $M_W > 6.9$ earthquake in the near future (Qian et al., 1988; Allen et al., 1991; Xiong et al., 2010). These seismic hazard analyses based on historical earthquake records and paleoseismic investigations are consistent with the inferences from our modeled results.

Furthermore, our modeled results show that the normal stress on the Xianshuihe fault varies significantly laterally and reaches the peak value in the north of Selaha and southwest of Moxi (Fig. 8a). Areas along the fault plane that have peaks of normal stress may act as barriers that halt

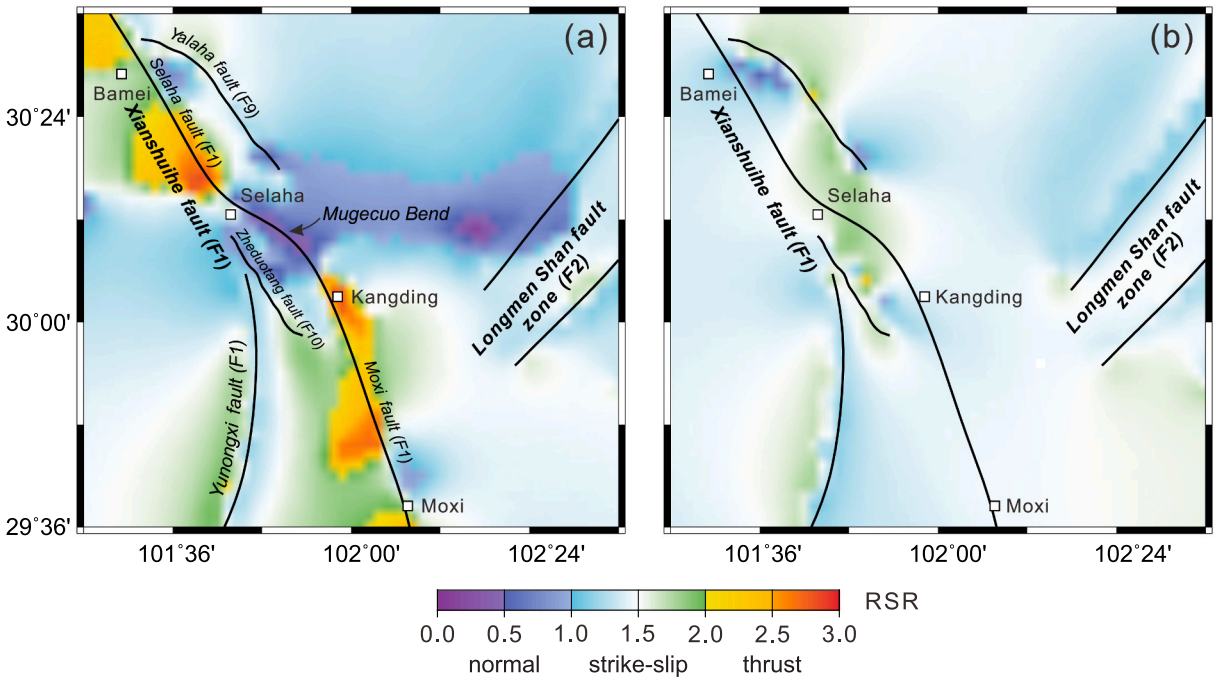

Fig. 9. Modeled regime stress ratio RSR in the corner of the Xianshuihe fault and the Longmen Shan fault zone. (a) All the faults can slip; (b) Only the Xianshuihe fault (i.e., Selaha fault segment and Moxi fault segment) is locked, other faults can slip. Comparison of the results of these two model tests indicates that the left-lateral slip of the Xianshuihe fault is the main cause of the normal faulting regime in the Mugecuo bend.

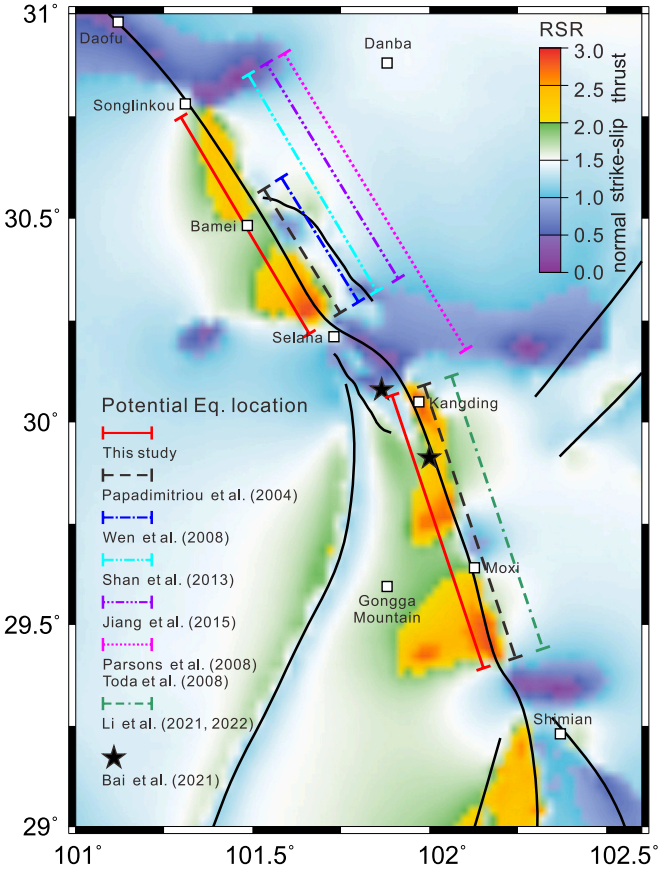

Fig. 10. The potential location of future large earthquakes in the Xianshuihe fault zone. The background colors indicate different stress regimes. The Songlinkou-Selaha segment and the Kangding-Bamei segment are considered to have high seismic hazards.

the propagating earthquake rupture. Therefore, we consider that the Xianshuihe fault tends to have segment-wise ruptures rather than an entire rupture along the whole 350 km long fault, which is consistent with previous studies (Cheng et al., 2020). However, it is difficult for us to conclude whether the rupture nucleated on the Songlinkou-Salaha segment or the Moxi fault in the future could pass through the Mugecuo releasing bend to form a larger earthquake. On one hand, field investigations showed that historical ruptures produced by the 1786 Kangding M 7.75 earthquake on the Moxi fault (Fig. 1) terminated at the Mugecuo bend (Wen et al., 2008). Dynamic models of earthquakes on the North Anatolian fault zone, which can be comparable to the Xianshuihe fault zone, also showed that the rupture nucleating near the releasing bend cannot pass through the bend (Oglesby et al., 2008). On the other hand, in Oglesby's earlier work, his conceptual dynamic models showed that the releasing bend was more prone to through-going rupture (Oglesby, 2005). The *b*-value analysis also suggested that the multi-segment rupture in the Bamei-Kangding segment is possible (Cheng et al., 2020). Therefore, it is appealed for the Xianshuihe fault, that the simulation of its scenario earthquake dynamic rupture propagation should be conducted, by considering a more realistic fault geometry model and stress state, rather than using simple fault geometry and an over-simplified stress state.

4.3. Potential of the Yulongxi fault for strong earthquakes

The Yulongxi fault (also known as "Yunongxi fault" in many previous publications), about 150 km long and NW-dipping, is the western boundary of Gongga Mountain (elevation is 7556 m), which is the highest peak in the eastern Tibetan Plateau. Roughly divided by the Yulongxi, the southern segment of the Yulongxi fault trends in NNE-SSW, and the northern segment trends S-N (Fig. 11). The sense of slip on the Yulongxi fault is currently under debate. Chen et al. (2016) used offset geomorphic features with their age data and determined that the Yulongxi fault is a left-lateral strike-slip fault with a slip rate of 3 mm/a. Jia et al. (1991) used the two-dimensional finite element method to simulate the kinematics of the Yulongxi fault and found that it is also a

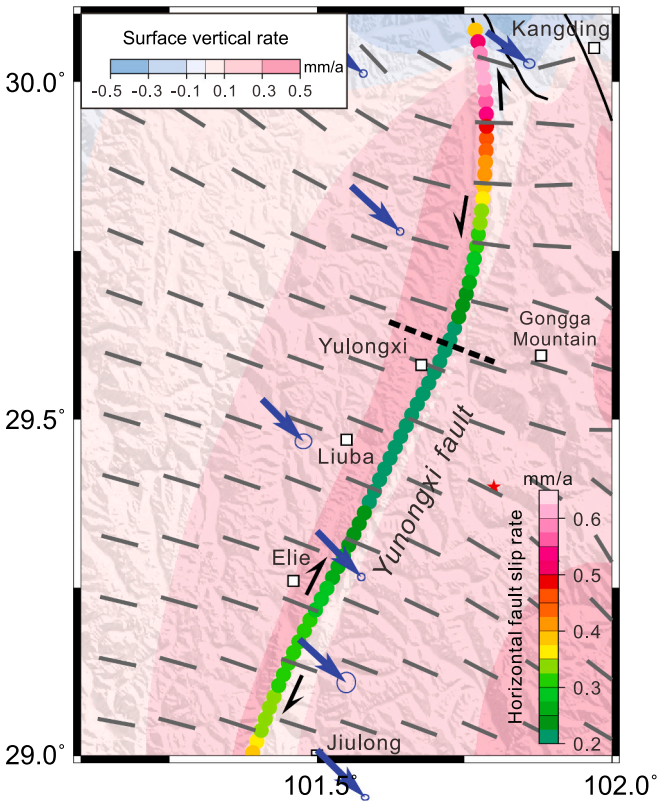

Fig. 11. Modeled horizontal fault slip rates and surface vertical velocities in the vicinity of the Yulongxi fault. Gray bars show the modeled S_H orientations. Blue arrows represent the GPS measurements (Wang and Shen, 2020). The dashed line shows the location of the boundary between the northern and southern segments of the Yulongxi fault. The location of this area is shown in Fig. 1. (For interpretation of the references to colour in this figure legend, the reader is referred to the web version of this article.)

left-lateral strike-slip fault with a slip rate of 1.3–1.7 mm/a. Huang et al. (2000) found that the Yulongxi fault did not obviously offset the alluvial fan, which is characterized by thrusting motion. Based on field surveys and combined with the striations on the fault surface, Zhang et al. (2011) divided the Yulongxi fault into two segments at Elie: the northern segment is thrusting with a left-lateral strike-slip component, while the southern segment is thrusting with a right-lateral strike-slip component (see Fig. 11). Our modeled results show that the slip rate of the Yulongxi fault is as low as 0.2–0.7 mm/a, and the uplift rate of the NW sidewall is 0.3–0.5 mm/a, which is higher than the 0.1 mm/a of the NE sidewall. Our results also demonstrate that the Yulongxi fault is a thrust fault with a slight strike-slip component. In addition, the modeled slip sense of the fault is reversed near Yulongxi. The northern segment is left-lateral strike-slip, while the southern segment is right-lateral strike-slip, which is consistent with the conclusions of Zhang et al. (2011) and Huang et al. (2000). The change in slip sense along the Yulongxi fault is presumed to be related to the change in its strike. The northern segment, which trends in near S-N, is prone to have a left-lateral strike-slip under the SE direction movement of the Sichuan-Yunnan block. While the southern segment, which trends in NNE-SSW, is more prone to have right-lateral slip under the E-W compression (Fig. 7a).

The Yulongxi fault has the potential to generate strong earthquakes. Zhang et al. (2009) considered that the strong deformation of the Bayan Har block, the high strength with a listric geometry of the Longmen Shan fault, and the obstruction of the rigid Sichuan Basin jointly formed the geological environment that contributed to the formation and occurrence of the 2008 Wenchuan M_S 8.0 earthquake. Zhang (2013) pointed out that faults with low slip rates can also be dangerous. The geological and geodynamic environment of the Yulongxi fault, which also slips slowly, is similar to that of the Longmen Shan fault zone. First, field investigations and magnetotelluric inversion results revealed that the Yulongxi fault is a thrust fault with a high dip angle, which is around 50–70° at shallow depth (Fig. S1). Such geometry is conducive to energy accumulation on the fault, especially when the S_H is nearly perpendicular to the fault strike direction (Fig. 11). In addition, the SE-ward crustal movement, revealed by the GPS measurements (Fig. 11), also promotes the energy accumulation process on the Yulongxi fault. Second, on the east side of the Yulongxi fault lies the Gongga Mountain, which is a Cenozoic granitic massif and the highest mountain in the eastern Qinghai-Tibet Plateau. This mountain can block the SE movement of crustal materials and further effectively support the stress accumulation on the Yulongxi fault. Finally, the Sichuan-Yunnan block, where the Yulongxi fault is located, moves southeastward at a rate of ~17 mm/a. This strong deformation provides the source of energy accumulation on the Yulongxi fault. This fault was developed in the Triassic lower metamorphic rocks and there are small-scale granite or diorite bodies outcropping along the fault, which may indicate that the rock of the Yulongxi fault is of high strength, thus the potential to gestate strong earthquakes. Proofs from paleoseismic investigations suggest that the recurrence interval of strong earthquakes of the Yunognxi fault is around 2000–2500 years (Gao, 2021), which is similar to that of the Longmen Shan fault zone (~3000 years) (Ran et al., 2013), and the elapsed time of the last large earthquake (~2600 years) (Gao, 2021) has been longer than the recurrence interval, thus we speculate that the Yulongxi fault may be of a high seismic hazard.

5. Conclusions

In this study, we have established a refined 3D geomechanical model of the Xianshuihe fault and its adjacent area by using more detailed geological and geodetic data. The model considers the complexity of updated 3D fault geometry and provides a spatially continuous contemporary kinematics and crustal background stress field for the study area.

For the kinematic results, the modeled slip rate on the Xianshuihe fault is as high as 11 mm/a in the northwest segment and decreases southeastward to ~9 mm/a near Moxi. The slip rate of the Litang fault is about 2 mm/a. The Yulongxi fault has different slip senses in different segments and its horizontal slip is as low as <0.6 mm/a.

For the stress state, the modeled S_H is generally oriented in the E-W direction and a transtensional faulting stress regime dominates the study area. The normal faulting regime in the Mugecuo bend is inferred to be caused by the extension of the Mugecuo pull-apart basin under the left-lateral strike-slip of the Xianshuihe fault, and it has already extended to the southwestern end of the Longmen Shan fault zone. The boundary strike-slip faults of the Mugecuo pull-apart basin are suggested to be the Selaha and Moxi faults.

The stress state on the Xianshuihe fault is inhomogeneous. Divided by Songlinkou, the normal stress on its southeastern segment is much higher than that on the northwestern segment. The thrust faulting stress regime on the Songlinkou-Selaha segment and the Moxi fault is inferred to result from the clockwise rotation of the fault strike. For these two segments, the high normal stress, as well as the relatively high slip rate, yields a relatively high seismic hazard. The similarity of the Yulongxi fault and the Longmen Shan fault zone in the geological and geodynamic environment suggests that the seismic activities of the Yulongxi fault should be paid close attention.

Supplementary data to this article can be found online at https://doi.org/10.1016/j.tecto.2022.229546.

Author-statement

Xianrui Li: Conceptualization, Investigation, Formal analysis, Writing - original draft **Ke Gao:** Funding acquisition, Project administration, Writing - review & editing **Yu Feng:** Writing - review & editing

Chongyuan Zhang: Writing - review & editing.

Declaration of Competing Interest

The authors declare that they have no known competing financial interests or personal relationships that could have appeared to influence the work reported in this paper.

Data availability

Data will be made available on request.

Acknowledgments

This work is supported by the Open Foundation of the United Laboratory of Numerical Earthquake Forecasting (Grant NO. 2020LNEF05), the China Postdoctoral Science Foundation (2021M691408) and the National Natural Science Foundation of China (NO. 41941018). We would like to thank editor Ramon Carbonell for managing the whole review process. We also thank three anonymous reviewers for their comments that helped us to improve the manuscript. Some figures were plotted using GMT (Wessel and Smith, 1998). The extraction of stress data from our model is by using the software GeoStress (Stromeyer et al., 2020).

References

Ahlers, S., Henk, A., Hergert, T., Reiter, K., Müller, B., Röckel, L., Heidbach, O., Morawietz, S., Scheck-Wenderoth, M., Anikiev, D., 2021. 3D crustal stress state of Western Central Europe according to a data-calibrated geomechanical model. Solid Earth 12, 1777–1799. https://doi.org/10.5194/se-12-1777-2021.

Allen, C.R., Zhuoli, L., Hong, Q., Xueze, W., Huawei, Z., Weishi, H., 1991. Field study of a highly active fault zone: the Xianshuihe fault of southwestern China. Geol. Soc. Am. Bull. 103, 1178–1199. https://doi.org/10.1130/0016-7606(1991)103%3C1178:FSOAHA%3E2.3.CO;2.

Armijo, R., Flerit, F., King, G., Meyer, B., 2004. Linear elastic fracture mechanics explains the past and present evolution of the Aegean. Earth Planet. Sci. Lett. 217, 85–95. https://doi.org/10.1016/S0012-821X(03)00590-9.

Bai, M., Chevalier, M.-L., Pan, J., Replumaz, A., Leloup, P.H., Métois, M., Li, H., 2018. Southeastward increase of the late Quaternary slip-rate of the Xianshuihe fault, eastern Tibet. Geodynamic and seismic hazard implications. Earth Planet. Sci. Lett. 485, 19–31. https://doi.org/10.1016/j.epsl.2017.12.045.

Bai, M., Chevalier, M.L., Leloup, P.H., Li, H., Pan, J., Replumaz, A., Wang, S., Li, K., Wu, Q., Liu, F., Zhang, J., 2021. Spatial slip rate distribution along the SE Xianshuihe fault, eastern Tibet, and earthquake hazard assessment. Tectonics 40. https://doi.org/10.1029/2021TC006985.

Brocher, T.M., 2005. Empirical relations between elastic wavespeeds and density in the earth's crust. Bull. Seismol. Soc. Am. 95, 2081–2092. https://doi.org/10.1785/0120050077.

Brotons, V., Tomás, R., Ivorra, S., Grediaga, A., Martínez-Martínez, J., Benavente, D., Gómez-Heras, M., 2016. Improved correlation between the static and dynamic elastic modulus of different types of rocks. Mater. Struct. 49, 3021–3037. https://doi.org/10.1617/s11527-015-0702-7.

Chen, G., Xu, X., Wen, X., Chen, Y.-G., 2016. Late quaternary slip-rates and slip partitioning on the southeastern Xianshuihe Fault system, Eastern Tibetan Plateau. Acta Geol. Sin. 90, 537–554. https://doi.org/10.1111/1755-6724.12689 (English Edition).

Cheng, J., Chartier, T., Xu, X., 2020. Multisegment rupture hazard modeling along the Xianshuihe Fault Zone, Southeastern Tibetan Plateau. Seismol. Res. Lett. 92, 951–964. https://doi.org/10.1785/0220200117.

Chevalier, M.-L., Leloup, P.H., Replumaz, A., Pan, J., Liu, D., Li, H., Gourbet, L., Métois, M., 2016. Tectonic-geomorphology of the Litang fault system, SE Tibetan Plateau, and implication for regional seismic hazard. Tectonophysics 682, 278–292. https://doi.org/10.1016/j.tecto.2016.05.039.

Deng, Q., Zhang, P., Ran, Y., Yang, X., Min, W., Chu, Q., 2003. Basic characteristics of active tectonics of China. Sci. China Earth Sci. 46, 356–372.

Fan, W., 1982. The geological tectonic foundation of Minya Gongkar and its characteristic glacial landforms. J. Chengdu Univ. Sci. Technol. 3, 19–33.

Fang, L., Wu, J., Liu, J., Cheng, J., Jiang, C., Han, L., Wang, Y., Chen, K., Zhao, X., Wu, Z., 2015. Preliminary Report on the 22 November 2014 Mw6.1/Ms6.3 Kangding Earthquake, Western Sichuan, China. Seismol. Res. Lett. 86, 1603–1613. https://doi.org/10.1785/0220150006.

Field, E.H., WGCEP, 2018. Improving earthquake rupture forecasts using California as a guide. Seismol. Res. Lett. 89, 2337–2346. https://doi.org/10.1785/0220180151.

Field, E.H., Biasi, G.P., Bird, P., Dawson, T.E., Felzer, K.R., Jackson, D.D., Johnson, K.M., Jordan, T.H., Madden, C., Michael, A.J., 2015. Long-term time-dependent probabilities for the third Uniform California Earthquake Rupture Forecast (UCERF3). Bull. Seismol. Soc. Am. 105, 511–543. https://doi.org/10.1785/0120140093.

Gan, W., Zhang, P., Shen, Z.-K., Niu, Z., Wang, M., Wan, Y., Zhou, D., Cheng, J., 2007. Present-day crustal motion within the Tibetan Plateau inferred from GPS measurements. J. Geophys. Res. 112, 1–14. https://doi.org/10.1029/2005JB004120.

Gao, S., 2021. Late Quaternary Paleoseismology and Faulting Behavior of the Internal and Western Boundary Faults of Northwest Sichuan Subblock. China Earthquake Administration, Beijing.

Gong, Y., He, Y., Wu, X., 1995. Discussion on the recent active feature of the Fubianhe fault. Sichuan Earthquake (4), 31–36.

He, J., Lu, S., 2007. Lower friction of the Xianshuihe-Xiaojiang fault system and its effect on active deformation around the south-eastern Tibetan margin. Terra Nova 19, 204–210. https://doi.org/10.1111/j.1365-3121.2007.00735.x.

Heidbach, O., Rajabi, M., Cui, X., Fuchs, K., Müller, B., Reinecker, J., Reiter, K., Tingay, M., Wenzel, F., Xie, F., Ziegler, M.O., Zoback, M.-L., Zoback, M., 2018. The World Stress Map database release 2016: crustal stress pattern across scales. Tectonophysics 744, 484–498. https://doi.org/10.1016/j.tecto.2018.07.007.

Hergert, T., 2009. Numerical Modelling of the Absolute Stress State in the Marmara Region - A Contribution to Seismic Hazard Assessment. Universität Karlsruhe, Karlsruhe. https://doi.org/10.5445/IR/1000012170.

Hergert, T., Heidbach, O., 2011. Geomechanical model of the Marmara Sea region—II. 3-D contemporary background stress field. Geophys. J. Int. 185, 1090–1102. https://doi.org/10.1111/j.1365-246X.2011.04992.x.

Hergert, T., Heidbach, O., Reiter, K., Giger, S.B., Marschall, P., 2015. Stress field sensitivity analysis in a sedimentary sequence of the Alpine foreland, northern Switzerland. Solid Earth 6, 533. https://doi.org/10.5194/se-6-533-2015.

Hu, X., Zang, A., Heidbach, O., Cui, X., Xie, F., Chen, J., 2017. Crustal stress pattern in China and its adjacent areas. J. Asian Earth Sci. 149, 20–28. https://doi.org/10.1016/j.jseaes.2017.07.005.

Huang, W., Zhou, R., He, Y., Li, X., 2000. Holocene activity on Yunongxi fault and Liuba M6.2 earthquake in Kangding, Sichuan. Earthquake Res. China 16, 53–59.

Hubert-Ferrari, A., King, G., Manighetti, I., Armijo, R., Meyer, B., Tapponnier, P., 2003. Long-term elasticity in the continental lithosphere; modelling the Aden Ridge propagation and the Anatolian extrusion process. Geophys. J. Int. 153, 111–132. https://doi.org/10.1046/j.1365-246X.2003.01872.x.

Jia, J., Wen, X., Pan, M., Liang, H., 1991. Numerical modeling of correlation between slip rate and fault geometry on the southeastern segment of the Xianshuihe fault zone. Earthquake Res. Sichuan 18–24.

Jiang, G., Xu, X., Chen, G., Liu, Y., Fukahata, Y., Wang, H., Yu, G., Tan, X., Xu, C., 2015. Geodetic imaging of potential seismogenic asperities on the Xianshuihe-Anninghe-Zemuhe fault system, southwest China, with a new 3-D viscoelastic interseismic coupling model. J. Geophys. Res. 120, 1855–1873. https://doi.org/10.1002/2014JB011492.

Jiang, F., Chen, X., Dong, Z., Cui, T., Liu, Z., Wang, P., 2019. Applying 3D inversion of single-profile magnetotelluric data to identify the Shade and Yunongxi faults. Seismol. Geol. 41, 1444–1463.

Laske, G., Masters, G., Ma, Z., Pasyanos, M., 2013. Update on CRUST1. 0—A 1-degree global model of Earth's crust. In: Geophysical Research Abstracts. EGU General Assembly Vienna, Austria, p. 2658.

Li, D., Chen, L., Liang, M., Gao, S., Zeng, D., Wang, H., Li, Y., 2017. Holocene palaeoseismologic record and rupture behavior of large earthquakes on the Xianshuihe fault. Seismol. Geol. 39, 623–643. https://doi.org/10.3969/j.issn.0253-4967.2017.04.001.

Li, J., Zhou, B., Li, T., Yang, Y., Li, Z., 2020. Locking depth, slip rate, and seismicity distribution along the Daofu–Kangding segment of the Xianshuihe fault system, eastern Tibetan Plateau. J. Asian Earth Sci. 193, 104328 https://doi.org/10.1016/j.jseaes.2020.104328.

Li, X., Hergert, T., Henk, A., Wang, D., Zeng, Z., 2019. Subsurface structure and spatial segmentation of the Longmen Shan fault zone at the eastern margin of Tibetan Plateau: evidence from focal mechanism solutions and stress field inversion. Tectonophysics 757, 10–23. https://doi.org/10.1016/j.tecto.2019.03.006.

Li, X., Hergert, T., Henk, A., Zeng, Z., 2021. Contemporary kinematics in the eastern Tibetan Plateau: insights from 3D geomechanical modeling. Tectonophysics 819, 229109. https://doi.org/10.1016/j.tecto.2021.229109.

Li, X., Hergert, T., Henk, A., Zeng, Z., 2022. Contemporary background stress field in the eastern Tibetan Plateau: insights from 3D geomechanical modeling. Tectonophysics 822, 229177. https://doi.org/10.1016/j.tecto.2021.229177.

Long, S., Zhao, Z., 2000. Characteristics of the seismic source stress field in the intersection region of Xianshuihe, Longmenshan and An'ninghe faults. Acta Seismol. Sin. 22, 457–464.

Lu, Renqi, 2019. The foult model in China Seismic Experimental Site, V1. CSES Scientific Products. (Accessed 22 August 2022).

Lund, B., Townend, J., 2007. Calculating horizontal stress orientations with full or partial knowledge of the tectonic stress tensor. Geophys. J. Int. 170, 1328–1335. https://doi.org/10.1111/j.1365-246X.2007.03468.x.

Ma, C., 2013. A Study of Fault Activity and Microtopography within the Chuandian Active blocks's Major Fault. Chendu University of Technology, Chengdu.

McGuire, R.K., 2004. Seismic Hazard and Risk Analysis. Earthquake Engineering Research Institute.

Molnar, P., Deng, Q., 1984. Faulting associated with large earthquakes and the average rate of deformation in central and eastern Asia. J. Geophys. Res. Solid Earth 89, 6203–6227. https://doi.org/10.1029/JB089iB07p06203.

Molnar, P., Lyon-Caent, H., 1989. Fault plane solutions of earthquakes and active tectonics of the Tibetan Plateau and its margins. Geophys. J. Int. 99, 123–153. https://doi.org/10.1111/j.1365-246X.1989.tb02020.x.

Oglesby, D.D., 2005. The dynamics of strike-slip step-overs with linking dip-slip faults. Bull. Seismol. Soc. Am. 95, 1604–1622. https://doi.org/10.1785/0120050058.
Oglesby, D.D., Mai, P.M., Atakan, K., Pucci, S., 2008. Dynamic models of earthquakes on the North Anatolian fault zone under the Sea of Marmara: effect of hypocenter location. Geophys. Res. Lett. 35 https://doi.org/10.1029/2008gl035037.
Pan, J., Li, H., Chevalier, M.-L., Bai, M., Liu, F., Liu, D., Zheng, Y., Lu, H., Zhao, Z., 2020. A newly discovered active fault on the Selaha-Kangding segment along the SE Xianshuihe fault: the South Mugecuo fault. Acta Geol. Sin. 94, 3178–3188. https://doi.org/10.19762/j.cnki.dizhixuebao.2020196.
Papadimitriou, E., Wen, X., Karakostas, V., Jin, X., 2004. Earthquake triggering along the Xianshuihe fault zone of Western Sichuan, China. Pure Appl. Geophys. 161, 1683–1707. https://doi.org/10.1007/s00024-003-2471-4.
Parsons, T., 2004. Recalculated probability of M≥ 7 earthquakes beneath the Sea of Marmara, Turkey. J. Geophys. Res. Solid Earth 109, B05304. https://doi.org/10.1029/2003JB002667.
Parsons, T., Ji, C., Kirby, E., 2008. Stress changes from the 2008 Wenchuan earthquake and increased hazard in the Sichuan basin. Nature 454, 509–510. https://doi.org/10.1038/nature07177.
Qian, H., Allen, C.R., Luo, Z., Wen, X., Zhou, H., Huang, W., 1988. The active characteristics of Xianshuihe fault in Holocene. Earthquake Res. China 4, 11–20.
Ran, Y.-K., Chen, W.-S., Xu, X.-W., Chen, L.-C., Wang, H., Yang, C.-C., Dong, S.-P., 2013. Paleoseismic events and recurrence interval along the Beichuan–Yingxiu fault of Longmenshan fault zone, Yingxiu, Sichuan, China. Tectonophysics 584, 81–90. https://doi.org/10.1016/j.tecto.2012.07.013.
Reiter, K., Heidbach, O., 2014. 3-D geomechanical–numerical model of the contemporary crustal stress state in the Alberta Basin (Canada). Solid Earth 5, 1123–1149. https://doi.org/10.5194/se-5-1123-2014.
Shan, B., Xiong, X., Wang, R., Zheng, Y., Yang, S., 2013. Coulomb stress evolution along Xianshuihe–Xiaojiang Fault System since 1713 and its interaction with Wenchuan earthquake, May 12, 2008. Earth Planet. Sci. Lett. 377–378, 199–210. https://doi.org/10.1016/j.epsl.2013.06.044.
Shen, Z.-K., Lü, J., Wang, M., Bürgmann, R., 2005. Contemporary crustal deformation around the southeast borderland of the Tibetan Plateau. J. Geophys. Res. 110, B11409. https://doi.org/10.1029/2004JB003421.
Sheorey, P.R., 1994. A theory for in situ stresses in isotropic and transversely isotropic rock. Int. J. Rock Mech. Min. Sci. Geomech. Abstr. 31, 23–34. https://doi.org/10.1016/0148-9062(94)92312-4.
Simpson, R.W., 1997. Quantifying Anderson's fault types. J. Geophys. Res. 102, 17909–17919. https://doi.org/10.1029/97JB01274.
Stromeyer, D., Heidbach, O., Ziegler, M., 2020. Tecplot 360 Add-on GeoStress, V2.0. GFZ Data Services. (Accessed 22 August 2022).
Tan, X., Xu, X., Li, Y., Chen, G., Wan, J., 2010. Apatite fission track evidence for rapid uplift of the Gongga Mountain and discussion of its mechanism. Chin. J. Geophys. 53, 1859–1867. https://doi.org/10.3969/j.issn.0001-5733.2010.08.011.
Taylor, M., Yin, A., 2009. Active Structures of the Himalayan-Tibetan Orogen and Their Relationships to Earthquake Distribution, Contemporary Strain Field, and Cenozoic Volcanism, 5, pp. 199–214. https://doi.org/10.1130/GES00217.1.
Toda, S., Lin, J., Meghraoui, M., Stein, R.S., 2008. May 2008 M = 7.9 Wenchuan, China, earthquake calculated to increase failure stress and seismicity rate on three major fault systems. Geophys. Res. Lett. 12, 35. https://doi.org/10.1029/2008GL034903.
Wang, X., 1992. A discussion on the structural breaks and their conditions in Xiaojin seismic area. Earthquake Res. Sichuan 24–32.
Wang, M., Shen, Z.K., 2020. Present-day crustal deformation of continental China derived from GPS and its tectonic implications. J. Geophys. Res. Solid Earth 125. https://doi.org/10.1029/2019JB018774.
Wang, C., Han, W., Wu, J., Lou, H., Bai, Z., 2003. Crustal structure beneath the Songpan-Garze orogenic belt. Acta Seismol. Sin. 16, 237–250. https://doi.org/10.1007/s11589-003-0028-3.
Wang, W., Qiao, X., Yang, S., Wang, D., 2017. Present-day velocity field and block kinematics of Tibetan Plateau from GPS measurements. Geophys. J. Int. 208, 1088–1102. https://doi.org/10.1093/gji/ggw445.
Wen, X., Ma, S., Xu, X., He, Y., 2008. Historical pattern and behavior of earthquake ruptures along the eastern boundary of the Sichuan-Yunnan faulted-block, southwestern China. Phys. Earth Planet. Inter. 168, 16–36. https://doi.org/10.1016/j.pepi.2008.04.013.
Wessel, P., Smith, W.H.F., 1998. New, improved version of Generic Mapping Tools released. Eos. Trans. AGU 79 (47), 579. https://doi.org/10.1029/98EO00426.
Xiong, T., Yao, X., Zhang, Y., 2010. A review on study of activity of Xianshuihe fault zone since the Holocene. J. Geom. 16, 176–188.
Xu, X., Wen, X., Ma, W., Song, F., Yu, G., 2003. Pattern of latest tectonic motion and its dynamics for active blocks in Sichuan-Yunnan region, China. Sci. China Earth Sci. 46, 210–226. https://doi.org/10.1360/03dz0017.
Xu, X., Zhang, P., Wen, X., Qin, Z., Chen, G., Zhu, A., 2005. Features of active tectonics and recurrence behaviors of strong earthquakes in the western Sichuan province and its adjacent regions. Seismol. Geol. 27, 446–461.
Yan, B., Lin, A., 2017. Holocene activity and paleoseismicity of the Selaha Fault, southeastern segment of the strike-slip Xianshuihe Fault Zone, Tibetan Plateau. Tectonophysics 694, 302–318. https://doi.org/10.1016/j.tecto.2016.11.014.
Yin, A., Harrison, T.M., 2000. Geologic evolution of the Himalayan-Tibetan orogen. Annu. Rev. Earth Planet. Sci. 28, 211–280. https://doi.org/10.1146/annurev.earth.28.1.211.
Zhang, P., 2013. Beware of slowly slipping faults. Nat. Geosci. 6, 323–324. https://doi.org/10.1038/ngeo1811.
Zhang, P., Yang, Z., Gupta, H.K., Bhatia, S.C., Shedlock, K.M., 1999. Global Seismic Hazard Assessment Program (GSHAP) in continental Asia. Ann. Geofis. 42, 1167–1190.
Zhang, P., Wen, X., Xu, X., Gan, W., Wang, M., Shen, Z., Wang, Q., Huang, Y., Zheng, Y., Li, X., 2009. Tectonic model of the great Wenchuan earthquake of May 12, 2008, Sichuan, China. Chin. Sci. Bull. 54, 944–953.
Zhang, J., Wu, D., Wang, D., 2011. Structural deformation and activity of the Bawolung-Yulongxi fracture zone in Jiulong, Sichuan. Acta Geol. Sichuan 31, 395–398.
Zhao, X., 1987. The sliding and tilting movements of Zheduoshan block in western Sichuan. J. Seismol. Res. 10, 459–466.
Zhou, R., He, Y., Huang, Z., Li, X., Yang, T., 2001. The Slip rate and strong earthquake recurrence interval on the Qianning-Kangding segment of the Xianshuihe fault zone. Acta Seismol. Sin. 23, 250–261. https://doi.org/10.3321/j.issn:0253-3782.2001.03.004.
Zoback, M.L., 1992. First- and second-order patterns of stress in the lithosphere: the world stress map project. J. Geophys. Res. 97, 11703. https://doi.org/10.1029/92JB00132.